ON THE MODULATION OF LOW-ORDER ROUGHNESSES ON THE FLOW OVER LOW-ORDER TOPOGRAPHIES

BY

MATIAS COLOMBO BAEZA

THESIS

Submitted in partial fulfillment of the requirements
for the degree of Master of Science in Mechanical Engineering
in the Graduate College of the
University of Illinois at Urbana-Champaign, 2019

Urbana, Illinois

Adviser:

Professor Leonardo Chamorro

ABSTRACT

The impact of low-order roughness on low-order topographies was experimentally explored using high-resolution particle image velocimetry in a refractive-index-matching channel at Reynolds numbers Re = 40,000, based on the channel half height and the bulk velocity. The topographies consisted on 2D and 3D sinusoidal waves, which spanned most of the test section. The roughnesses also consisted on the same waveforms but one order of magnitude smaller than the topographies. We focused on 2D-2D and 3D-3D roughness-topography configurations. The flow statistics are compared with hydrodynamically smooth wavy topographies to get insight on the effects of the 2D and 3D roughnesses. Inspection of the flow statistics reveal that the low-order roughness induced changes in the velocity fluctuations near the wall; mean flow was not substantially modified. In particular, the Reynolds stress decomposition via quadrant analysis revealed that the 2D roughness reduced the sweeps and ejections in the 2D topography; however, negligible changes occurred in the 3D case. Inspection of the flow fluctuations with Proper orthogonal decomposition at various spatial regions revealed that the 3D roughness increased the complexity of the flow, attributed possibly to the generation of small-scale motions located within the troughs.

ACKNOWLEDGEMENTS

This work was supported by the Department of Mechanical Science and Engineering, University of Illinois at Urbana-Champaign, as part of the start-up package of Leonardo P. Chamorro. The experiments were performed in a facility built under the National Science Foundation grant award CBET-0923106.

TABLE OF CONTENTS

CHAPTER 1: INTRODUCTION

Characterization of the flow over topographies is pivotal to understand and control mixing, dispersion and particle transport in environmental and engineering flows. A variety of natural terrains exhibits low-order complexity, which are shaped by a number of factors, including wind-driven erosion and rain. Interestingly, some of those low-order topographies also exhibit low-order roughness; desert dunes with ripples are outstanding examples. In those cases, the specific role of ripples on the dynamics of near-wall and boundary layer turbulence remains unclear.

Sinusoidal walls have been used as idealized configurations to uncover dominant features of the flow over topographies. Early works inspected various phenomena including the recirculation regions over smooth wavy walls (e.g., Zilker *et al.* 1977; Zilker & Hanratty 1979; Buckles *et al.* 1984), the effect of aspect ratio, namely the wave height to wavelength (e.g., Kuzan *et al.* 1989; Yoon *et al.* 2009), the turbulence in the inner and outer regions (Nakagawa & Hanratty 2001; Hudson *et al.* 1996; Bhaganagar *et al.* 2004), turbulent momentum transport (Kuhn *et al.* 2007) and heat transfer (e.g., Choi & Suzuki 2005; Kuhn & von Rohr 2008; Wagner *et al*. 2011; Kuhn *et al*. 2010) among others. A comprehensive discussion on the flow over wavy walls can be found in Belcher & Hunt (1998).

Experiments using PIV have provided particular insight on the flow over wavy surfaces. For instance, Günther & Von Rohr (2003) identified longitudinal structures with a characteristic length scales larger than the wall wavelength and inspection with POD revealed that few modes contained the bulk of the energy. PIV-based POD from Kruse *et al.* (2006) showed the important role of large-scale motions in the transport of momentum. Recently, Segunda *et al.* (2016) discussed the location of fully periodic flow. Hamed *et al.* (2016) investigated the laminar-to-

turbulence transition over 2D and 3D wavy walls and found that occurred earlier in the 2D wavy wall; they attributed such phenomenon to the presence of a velocity inflection point from flow separation. They also found that the transitional region was characterized by the interaction between above- and near-roughness disturbances, which led to rapid vertical growth of the turbulent fluctuations. Hamed *et al.* (2015) studied the response of turbulent boundary layer to 2D and 3D wavy walls, and found that the spanwise variability of the 3D topography led to a much milder response, namely, the boundary layer thickness and integral parameters.

In this work, we experimentally study the potential impact of 2D and 3D sinusoidal roughness on 2D and 3D sinusoidal topographies. We use very-high-resolution PIV in a refractive-index-matching channel to characterize the flow statistics within a wall-normal plane. The experimental set-up is described in §2; the experimental measurements are analyzed and discussed in §3; and the conclusions of this work are presented in §4.

CHAPTER 2: EXPERIMENTAL SETUP

Laboratory experiments were carried out to characterize the impact of low-order roughnesses on the flow over hydrodynamically smooth, low-order topographies under developed flow conditions. The measurements were made in a 2.5 m long, 112.5 × 112.5 mm^2 cross section closed-loop, refractive-index-matching (RIM) channel. The base topographies consisted on 2D and 3D sinusoidal waves given by:

$$\sigma_{2D}(x) = A_T \cos\left(\frac{2\pi x}{\lambda_{xT}}\right) \quad \text{and} \quad \sigma_{3D}(x,y) = A_T \cos\left(\frac{2\pi x}{\lambda_{xT}}\right) \cos\left(\frac{2\pi y}{\lambda_{yT}}\right) \tag{2.1}$$

where A_T = 5 mm, λ_{xT} = 100 mm and $\lambda_{yT}/\lambda_{xT}$ = 1/2, which resulted in amplitude to wavelength ratios of A_T/λ_{xT} = 0.05 and A_T/λ_{yT} = 0.1. A 2D roughness with amplitude and wavelength of A_r/A_T = 1/10 and $\lambda_{xr}/\lambda_{xT}$ = 1/13 was superimposed over the 2D topography. Similarly, a 3D roughness with amplitude A_r and wavelengths $\lambda_{xr}/\lambda_{xT} = \lambda_{yr}/\lambda_{yT}$ = 1/13 was superimposed to the 3D topography. Then, the equations of the 2D topography with 2D roughness (henceforth 2D2D) and the 3D topography with 3D roughness (henceforth 3D3D) are:

$$\sigma_{2D2D}(x) = A_T \cos\left(\frac{2\pi x}{\lambda_{xT}}\right) + A_r \cos\left(\frac{2\pi x}{\lambda_{xr}}\right) \tag{2.2}$$

$$\sigma_{3D3D}(x,y) = A_T \cos\left(\frac{2\pi x}{\lambda_{xT}}\right) \cos\left(\frac{2\pi y}{\lambda_{yT}}\right) + A_r \cos\left(\frac{2\pi x}{\lambda_{xr}}\right) \cos\left(\frac{2\pi y}{\lambda_{yr}}\right)$$

The four surfaces topographies, $\sigma_{2D}(x)$; $\sigma_{2D2D}(x)$; $\sigma_{3D}(x,y)$ and $\sigma_{3D3D}(x,y)$, are illustrated in figure 1. They covered most of the test section and were preceded by a short flat plate with an elliptical leading edge. The topographies were cast from urethane resins using hydrodynamically smooth molds. A NaI aqueous solution of ~63% by weight, density ρ = 1800 kg m^{-3} and a kinematic viscosity ν = 1.1 × 10^{-6} m^2 s^{-1}, was used as a working fluid. The refractive index of the solution was fine tuned to match that of the wall using temperature

control; this made the walls nearly invisible and allowed flow measurements in the thoughts and very near the wall. For additional information about this technique, see the works Bai & Katz (2014) and Blois *et al.* (2012).

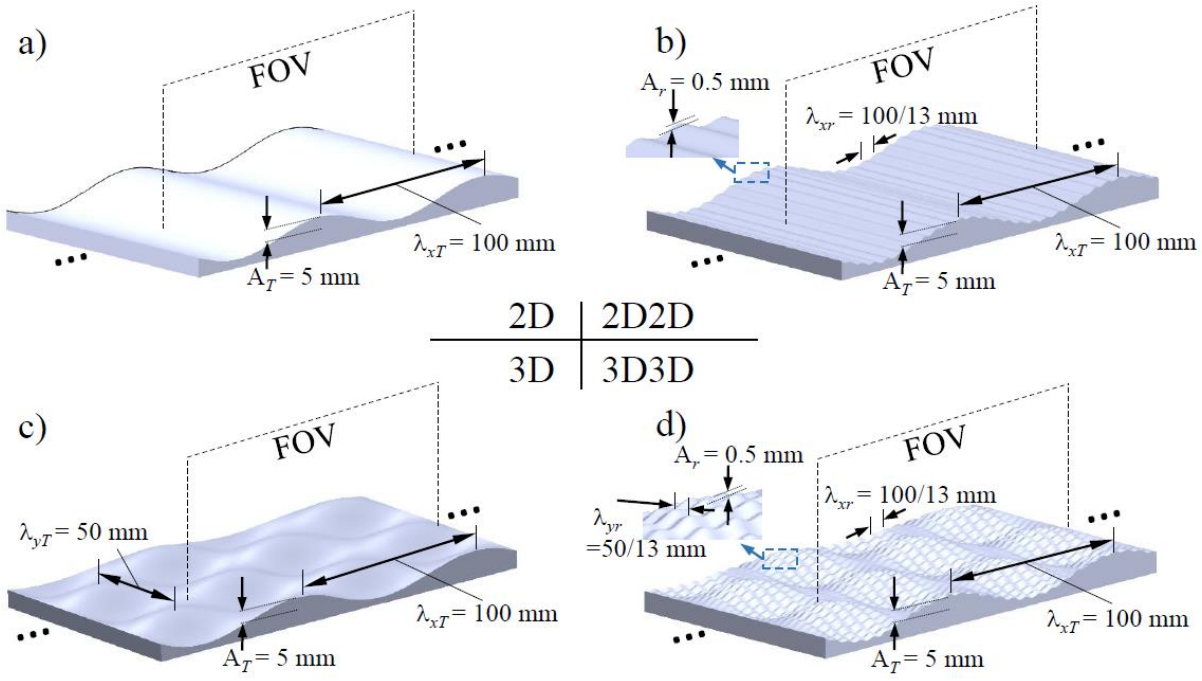

Figure 1: Basic dimensions of the sinusoidal walls with low-order topographies and low order roughnesses. a) Smooth 2D topography, b) 2D topography with 2D roughness, c) smooth 2D topography, d) 3D topography with 3D roughness.

Flow statistics were inspected at a Reynolds number based on the bulk velocity and channel half-height of $Re = 4 \times 10^4$; this is the same condition of related studies by Hamed *et al.* (2015).

The flow was seeded with 14 μm silver coated hollow glass spheres tracer particles, with a density of 1700 kg m^{-1}, and characterized with a high-resolution particle image velocimetry (PIV) within a wall-normal plane in the developed region extending over a wavelength. A field of view (FOV) of 160 mm × 107 mm was illuminated with a 1 mm thick laser sheet using a 250 mJ $pulse^{-1}$ double-pulsed laser from Quantel. For each scenario, four thousand image pairs were

collected at a frequency of 1 Hz with a 29 MP, 12 bit, frame-straddle, CCD camera. A recursive cross-correlation method was applied to interrogate the image pairs via Insight 4G software from TSI. The final interrogation window had a size of 24 pixels × 24 pixels with 50% overlap, resulting in a vector grid spacing of $\Delta x = \Delta y \approx 200$ μm and 300 μm.

CHAPTER 3: RESULTS

In this section we show and discuss the effect of the low-order roughness on the low-order topographies described in §2. Vertical planes within the developed region as well as one-dimensional profiles of the first- and second-order turbulence statistics, quadrant analysis and snapshot proper orthogonal decomposition (POD) are used to assess the roughness modulation.

First, qualitative insight on the impact of the low-order roughness on the 2D and 3D topographies is obtained by inspecting instantaneous, representative fields of the velocity fluctuations, which are illustrated in figure 2. There, streamwise fluctuations u'/U_b are superimposed to the vector field to highlight flow features. All the cases show largescale regions of positive and negative velocity fluctuations; however, those with the wavy roughness exhibit small-scale regions of alternating velocity fluctuations near the wall, roughly within $\Delta z/H \lesssim 0.1$. This is particularly evident in the 2D2D case (figure 2b). This small-scale effect may modulate the energy distribution, spectrum of scales and near-wall dynamics of the topographies, as discussed later.

Despite the distinct features induced by the roughness, the mean streamwise velocity did not undergo significant changes (fig. 3); this was also the case for the vertical component (not shown for brevity, included in APPENDIX B). This indicates that the effects of the low-order roughness, if any, may be mostly related to the (re-)distribution and production of the turbulence near the wall. Indeed, the Reynolds stresses, in particular the kinematic shear stress $\langle u'w' \rangle/U_b$ is affected only near the wall and around the through of the 2D2D topography. Selected vertical profiles every $\Delta x/\lambda_{xT} = 0.1$ shown in figure 4 evidence such effect. Changes associated to the low-order roughness are contained in the adverse pressure gradient section $\left(\Delta x/\lambda_{xT} \in (0.2, 0.5)\right)$, and resulted in a reduction of the stress.

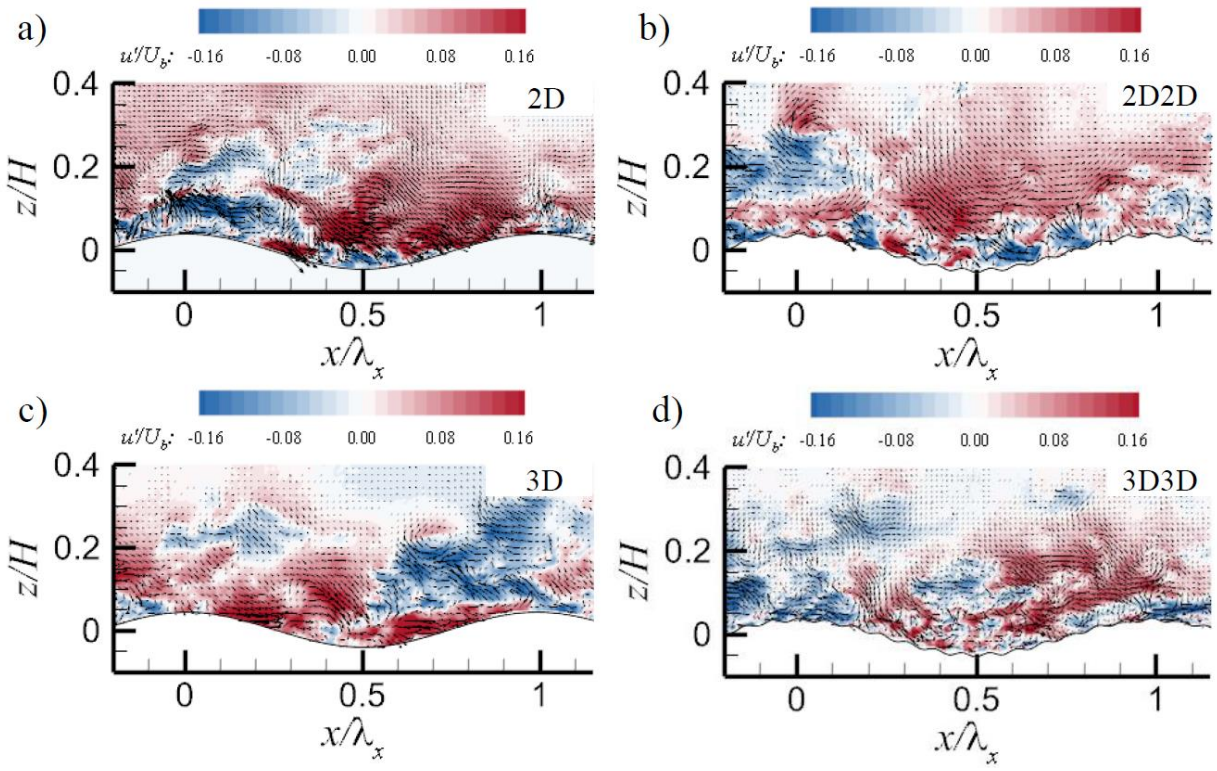

Figure 2: Instantaneous fields of velocity fluctuations $\boldsymbol{u'i + w'k}$ superimposed on contours of $\boldsymbol{u'/U_b}$ for the a) 2D, b) 2D2D, c) 3D and d) 3D3D topographies. For clarity, the figures only show every four vectors.

Remarkably, the 3D topography was not affected as shown in figure 5; the differences were negligible. Inspection with the quadrant decomposition, namely, ejection ($Q2: u' < 0 \; and \; w' > 0$) and sweeps ($Q4: u' > 0 \; and \; w' < 0$) events as well as inward ($Q3: u' < 0 \; and \; w' < 0$) and outward ($Q1: u' > 0 \; and \; w' > 0$) interactions reveals that the reduction of the near-wall shear stress in the 2D2D topography is associated to a reduction of sweeping and ejection events (fig. 6); external interactions remained nearly similar (not shown here). Same decomposition for the 3D case did not show such redistribution of $u'w'$.

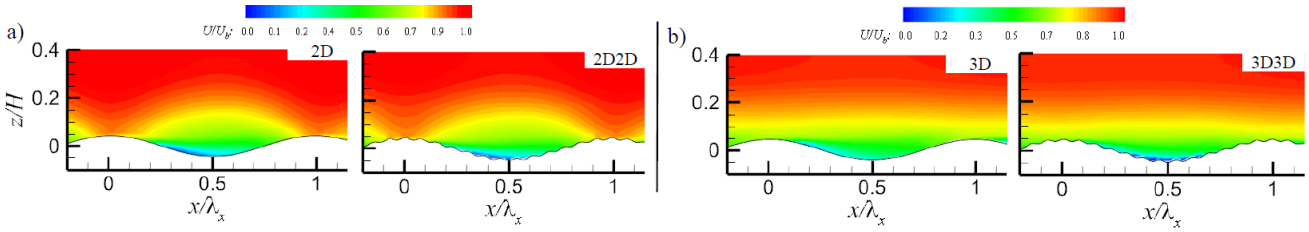

Figure 3: Non-dimensional time-averaged streamwise velocity fields $\boldsymbol{U/U_b}$ of the a) 2D and 2D2D topographies and b) 3D and 3D3D topographies.

The in-plane, time-averaged TKE production rate E_{tk} given by (Hudson *et al.* 1996; Kruse *et al.* 2006):

$$E_{tk} = -\langle u'w' \rangle \frac{\partial U}{\partial z} - \langle u'^2 \rangle \frac{\partial U}{\partial x} - \langle u'w' \rangle \frac{\partial W}{\partial x} - \langle w'^2 \rangle \frac{\partial W}{\partial z} \tag{3.1}$$

illustrates distinct effects of the wavy roughness on the near-wall flow, as shown in figure 7. Locally enhanced levels of E_{tk} occurred in the lower pressure side of each roughness wave, which is similar to that occurring in the lower pressure side of the topography. The roughness-induced E_{tk} appears to induce only a very local effect; however, it may trigger the generation of

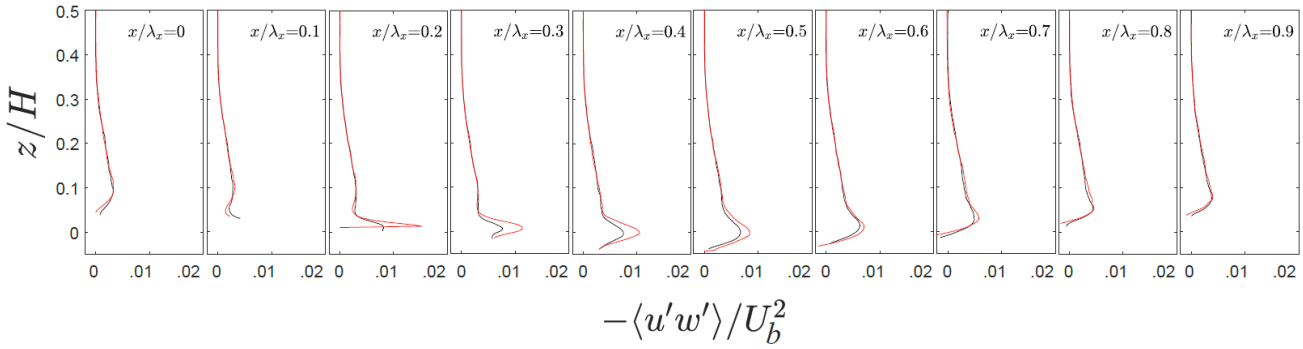

Figure 4: Vertical profiles of the kinematic shear stress $\boldsymbol{\langle u'w' \rangle / U_0}$ at selected locations along the 2D (red), and 2D2D (black) topographies.

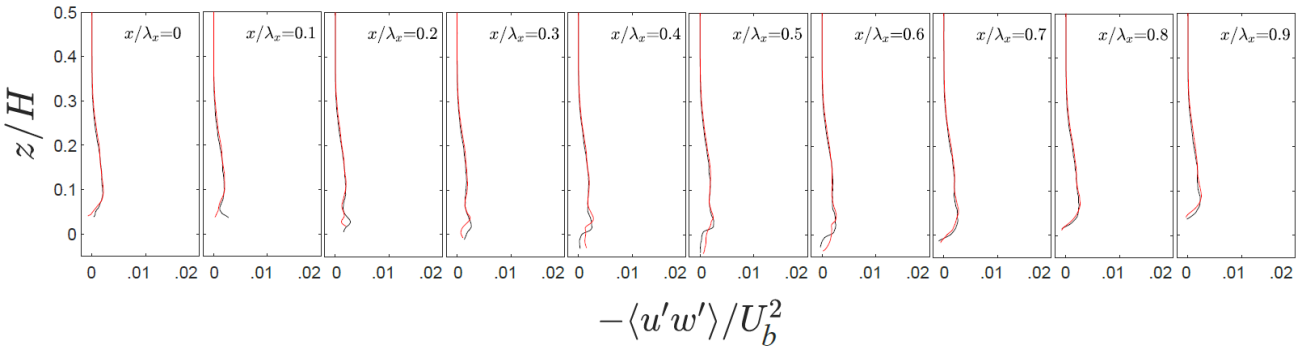

Figure 5: Vertical profiles of the kinematic shear stress $\langle \boldsymbol{u'w'} \rangle / \boldsymbol{U_0}$ at selected locations along the 3D (red), and 3D3D (black) topographies.

small-scale coherent motions. This is inspected with the decomposition of the flow via proper orthogonal decomposition (POD). For this purpose, we inspected 4,000 snapshots of the fluctuating velocity fields following Sirovich (1987) for the four cases. The dominant spatial features of the flow field is obtained by decomposing the fluctuating velocity signal $u'(x,t)$ into a deterministic part $\Phi^n(x)$ (POD modes) and time-dependent coefficients $a^n(t)$ as follows:

$$u'(x,t) = \sum_{n=1}^{10,000} a^n(t)\Phi^n(x) \qquad (3.1)$$

To gain additional insight on the modulation of the roughness on the energetic modes and the spatial extent, we additionally considered spatial regions with vertical spans ranging from the wall to $z/H = 0.3$, 0.1 and 0.05. Note that this last case correspond to the region within the troughs.

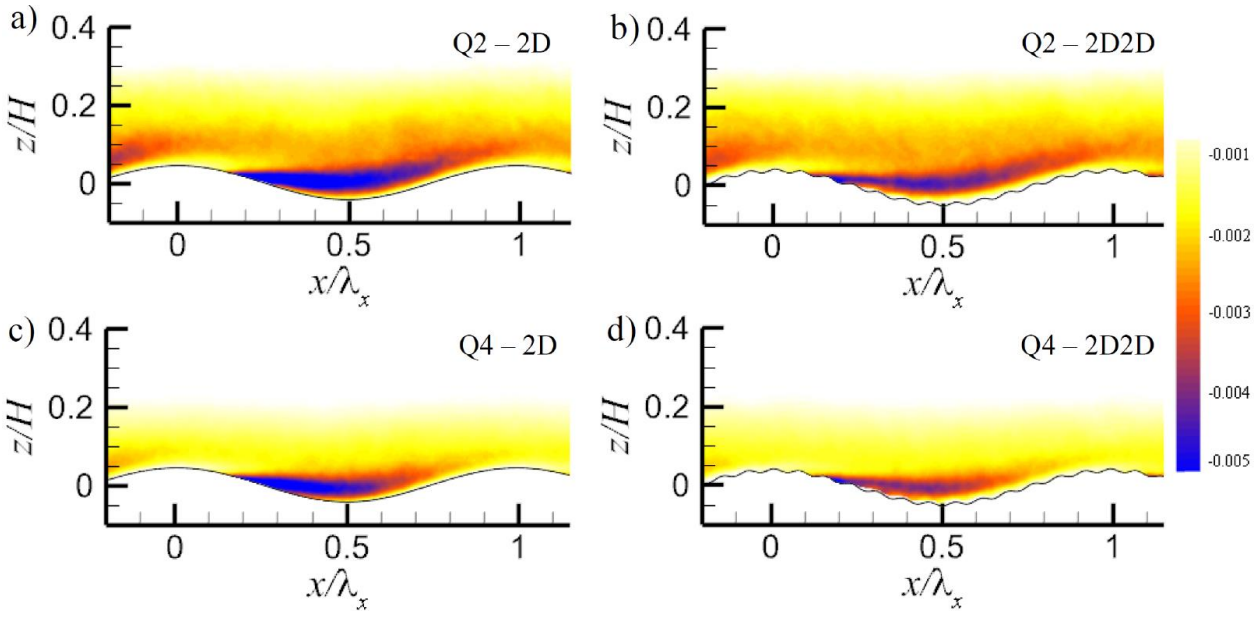

Figure 6: Quadrant decomposition of the kinematic shear stress $\boldsymbol{u'w'}$. Ejection events (Q2) for the a) 2D and b) 2D2D cases: sweeps (Q4) events for the c) 2D and d) 2D2D cases.

The analysis is summarized in figure 8. It reveals distinct roughness modulation depending on the number of topographical modes. Regardless of the spatial domain, the flow fluctuations over the 2D2D topography exhibited larger energy content for a given number of modes with respect to the smooth case. Opposite phenomenon occurred with the 3D3D case. Inspection of the energy distribution with different regions shows the comparatively larger effect of the 3D roughness. Indeed, it significantly affected the turbulent energy within the troughs of the 3D3D roughness.

This is illustrated in figure 8.c; for instance, to achieve 75% of the energy of the flow within the troughs ($z/H = 0.05$) , it is required ≈ 55 modes in the smooth case, but ≈ 90 modes with the 3D roughness. This difference reduced with increased vertical extent. Finally, the changes in the 2D topographies are not substantial.

CHAPTER 4: CONCLUDING REMARKS

The laboratory inspection of the low-order roughness effects on the low-order topographies evidenced local modulation near the wall, which affected the velocity fluctuations and the energy content. Interestingly, such effects were different in the 2D and 3D topographies. This is the case for the Reynolds stress decomposition and POD. Indeed, the 2D roughness

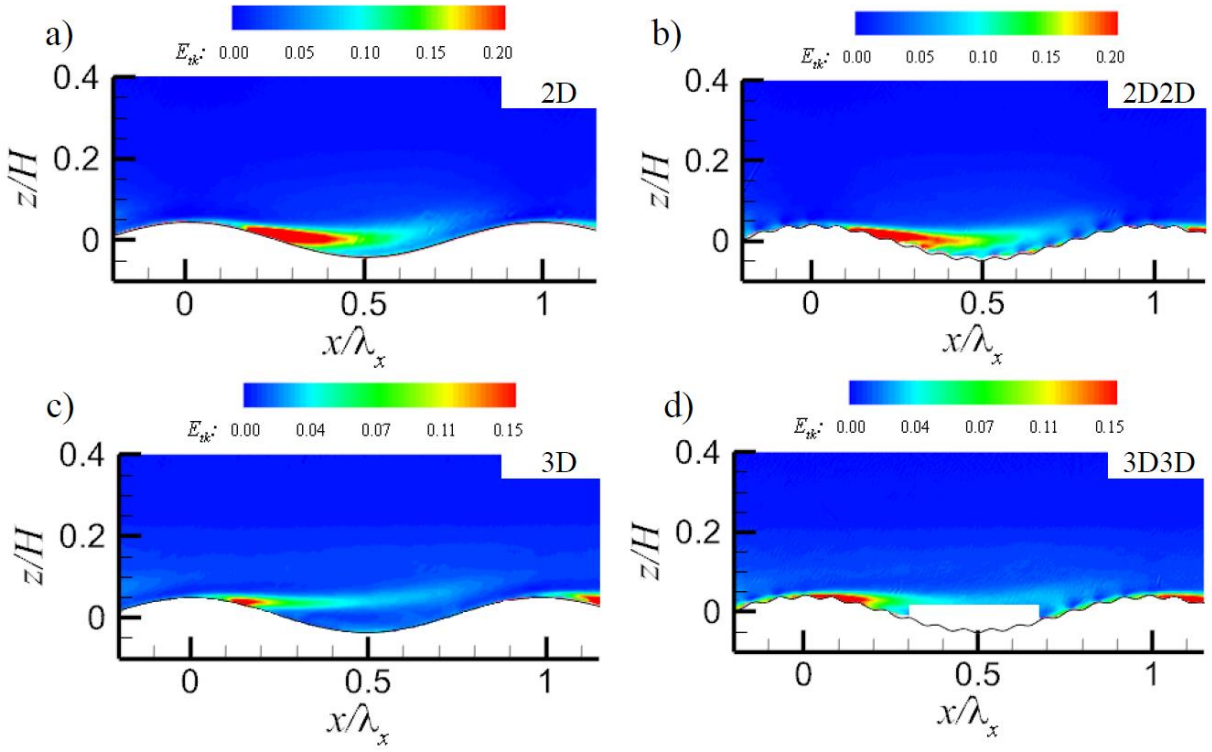

Figure 7: In-plane turbulence kinetic energy production, $\boldsymbol{E_{tk}}$, for the a) 2D, b) 2D2D, c) 3D and d) 3D3D topographies.

reduced the sweeps and ejections in the 2D topography; however, negligible changes occurred with the 3D roughness in the 3D topography. The POD showed that the 2D roughness slightly reduced the number of modes needed to get the same energy as the 2D2D topography; however, opposite phenomenon occurred with the 3D roughness in the 3D topography.

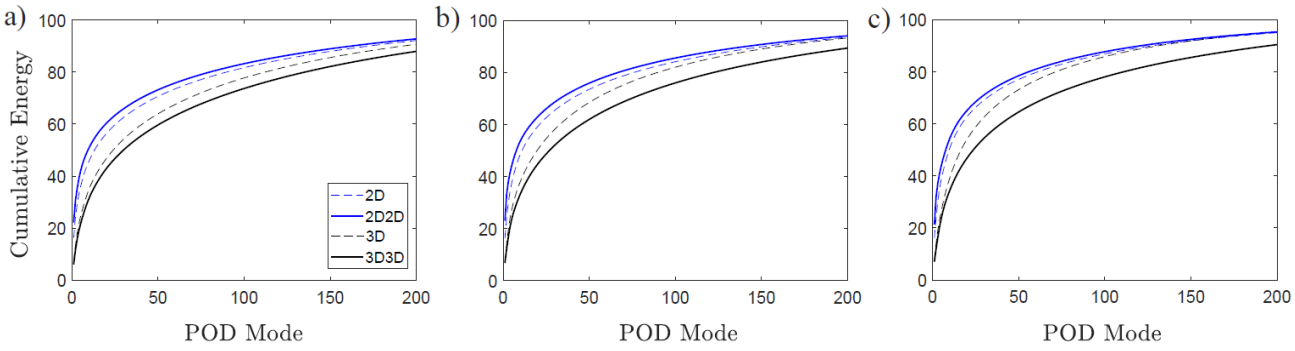

Figure 8: POD modes of the streamwise velocity fluctuations $\boldsymbol{\Phi_{u'}}$ for all the cases considering regions with vertical extents of $\boldsymbol{z/H}$ = a) 0.3, b) 0.1 and c) 0.05.

REFERENCES

Bai, K. & Katz, J. 2014 On the refractive index of sodium iodide solutions for index matching in piv. *Exp. Fluids* 55, 1-6.
https://link.springer.com/article/10.1007/s00348-014-1704-x

Belcher, S. E. & Hunt, J. C. R. 1998 Turbulent flow over hills and waves. *Annu Rev Fluid Mech* 30 (1), 507-538.
https://www.annualreviews.org/doi/abs/10.1146/annurev.fluid.30.1.507

Bhaganagar, K., Kim, J. & Coleman, G. 2004 Effect of roughness on wall-bounded turbulence. *Flow Turbul Combust* 72 (2-4), 463-492.
https://link.springer.com/article/10.1023/B:APPL.0000044407.34121.64

Blois, Gianluca, Christensen, Kenneth, Best, James, Elliott, Gregory, Austin, Joanna, Dutton, J Craig, Bragg, Michael, Garcia, Marcelo & Fouke, Bruce 2012 A versatile refractive-index-matched ow facility for studies of complex ow systems across scientific disciplines p. 736.
https://arc.aiaa.org/doi/pdf/10.2514/6.2012-736

Buckles, J., Hanratty, T. J. & Adrian, R. J. 1984 Turbulent flow over large-amplitude wavy surfaces. *J Fluid Mech* 140, 27-44.
https://www.cambridge.org/core/journals/journal-of-fluid-mechanics/article/turbulent-flow-over-largeamplitude-wavy-surfaces/1994AC7D029BFEE11B4DB9A7272C0303

Choi, Hang Seok & Suzuki, Kenjiro 2005 Large eddy simulation of turbulent flow and heat transfer in a channel with one wavy wall. *Int. J. Heat Fluid Fl.* 26 (5), 681-694.
https://www.sciencedirect.com/science/article/pii/S0142727X05000275

Günther, Axel & Von Rohr, Philipp Rudolf 2003 Large-scale structures in a developed flow over a wavy wall. J. fluid Mech. 478, 257-285.
https://www.cambridge.org/core/journals/journal-of-fluid-mechanics/article/largescale-structures-in-a-developed-flow-over-a-wavy-wall/DF5C68350F107DBCE62F80991546DA5D

Hamed, A. M., Kamdar, A., Castillo, L. & Chamorro, L. P. 2015 Turbulent boundary layer over 2d and 3d large-scale wavy walls. *Phys Fluids* 27 (10), 106601.
https://aip.scitation.org/doi/abs/10.1063/1.4933098

Hamed, A. M., Sadowski, M., Zhang, Z. & Chamorro, L. P. 2016 Transition to turbulence over 2d and 3d periodic large-scale roughnesses. *J Fluid Mech* 804, R6, 1-12.
https://www.cambridge.org/core/journals/journal-of-fluid-mechanics/article/transition-to-turbulence-over-2d-and-3d-periodic-largescale-roughnesses/16F162AA7743B4314986FD8868E8F2ED

Hudson, J. D., Dykhno, L. & Hanratty, T. J. 1996 Turbulence production in flow over a wavy wall. *Exp. Fluids* 20 (4), 257-265.
https://link.springer.com/article/10.1007/BF00192670

Kruse, N., Kuhn, S. & von Rohr, P. R. 2006 Wavy wall effects on turbulence production and large-scale modes. *J. Turbul*. 7, no. 31.
https://www.tandfonline.com/doi/abs/10.1080/14685240600602911

Kuhn, Simon, Kenjereš, Saša & von Rohr, Philipp Rudolf 2010 Large eddy simulations of wall heat transfer and coherent structures in mixed convection over a wavy wall. *Int. J. Therm. Sci*. 49 (7), 1209-1226.
https://www.sciencedirect.com/science/article/pii/S1290072910000426

Kuhn, Simon & von Rohr, Philipp Rudolf 2008 Experimental study of heat flux in mixed convective flow over solid waves. *Exp. Fluids* 44 (6), 973-984.
https://link.springer.com/article/10.1007/s00348-007-0456-2

Kuhn, Simon, Wagner, Carsten & von Rohr, Philipp Rudolf 2007 Influence of wavy surfaces on coherent structures in a turbulent flow. *Exp. Fluids* 43 (2-3), 251-259.
https://link.springer.com/article/10.1007/s00348-007-0262-x

Kuzan, J. D., Hanratty, T. J. & Adrian, R. J. 1989 Turbulent flows with incipient separation over solid waves. *Exp. Fluids* 7, 88-98.
https://link.springer.com/article/10.1007/BF00207300

Nakagawa, S. & Hanratty, T. J. 2001 Particle image velocimetry measurements of flow over a wavy wall. *Phys. of Fluids* 13, 3504-3507.
https://aip.scitation.org/doi/abs/10.1063/1.1399291

Segunda, Vinicius Martins, Tachie, Mark & Ormiston, Scott 2016 Piv investigation of turbulent flow over a wavy-wall in a horizontal channel. In *ASME 2016 Fluids Engineering Division Summer Meeting*, pp. V002T10A001-V002T10A001. American Society of Mechanical Engineers.
https://proceedings.asmedigitalcollection.asme.org/proceeding.aspx?articleid=2591125

Sirovich, Lawrence 1987 Turbulence and the dynamics of coherent structures. i. coherent structures. *Quarterly of applied mathematics* 45 (3), 561-571.
https://www.ams.org/journals/qam/1987-45-03/S0033-569X-1987-0910462-6/S0033-569X-1987-0910462-6.pdf

Wagner, Carsten, Kenjereš, Saša & von Rohr, Philipp Rudolf 2011 Dynamic large eddy simulations of momentum and wall heat transfer in forced convection over wavy surfaces. *J. Turbul.* (12), N7.
https://www.tandfonline.com/doi/abs/10.1080/14685248.2010.547496

Yoon, HS, El-Samni, OA, Huynh, AT, Chun, HH, Kim, HJ, Pham, AH & Park, IR 2009 Effect of wave amplitude on turbulent flow in a wavy channel by direct numerical simulation. *Ocean Eng*. 36 (9-10), 697-707.
https://www.sciencedirect.com/science/article/pii/S0029801809000869

Zilker, D. P., Cook, G. W. & Hanratty, T. J. 1977 Influence of the amplitude of a solid wavy wall on a turbulent flow. part 1. non-separated flows. *J Fluid Mech* 82, 29-51. https://www.cambridge.org/core/journals/journal-of-fluid-mechanics/article/influence-of-the-amplitude-of-a-solid-wavy-wall-on-a-turbulent-flow-part-1-nonseparated-flows/27F9DDE5FC1DF1EA3D5CB10B9EC0A0AD

Zilker, D. P. & Hanratty, T. J. 1979 Influence of the amplitude of a solid wavy wall on a turbulent flow. part 2. separated flows. *J Fluid Mech* 90, 257-271. https://www.cambridge.org/core/journals/journal-of-fluid-mechanics/article/influence-of-the-amplitude-of-a-solid-wavy-wall-on-a-turbulent-flow-part-2-separated-flows/0B6ACA2C76A2150B27A470AA21D8CACE

APPENDIX A: CASES AT REYNOLDS NUMBER OF 4000

Figure 9: Non-dimensional time-averaged streamwise velocity fields $\boldsymbol{U/U_b}$ of the a) 2D, b) 2D2D, c) 3D and d) 3D3D topographies, at Reynolds number of 4000.

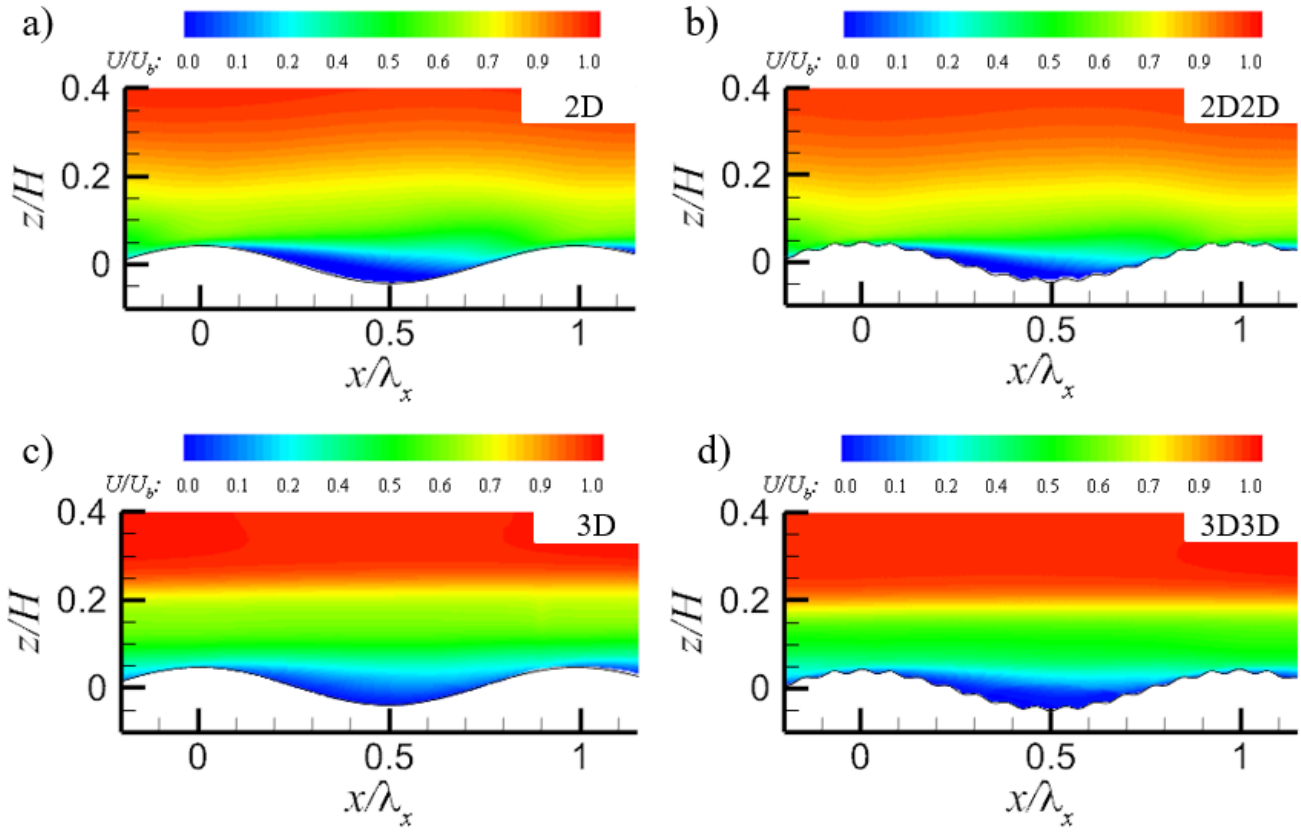

Figure 10: Non-dimensional time-averaged spanwise velocity fields $\boldsymbol{W/U_b}$ of the a) 2D, b) 2D2D, c) 3D and d) 3D3D topographies, at Reynolds number of 4000.

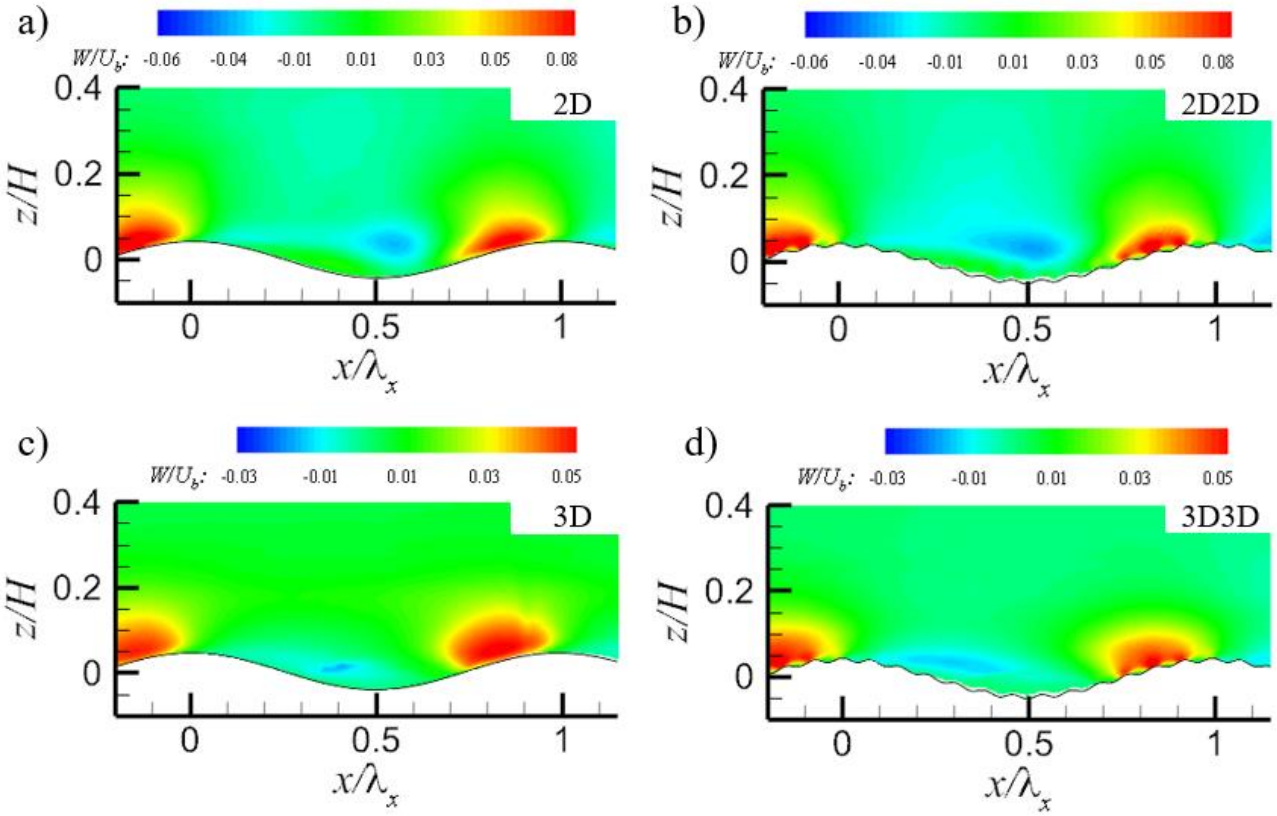

Figure 11: Reynolds shear stress $-\langle u'w'\rangle/U_b^2$ of the a) 2D, b) 2D2D, c) 3D and d) 3D3D topographies, at Reynolds number of 4000.

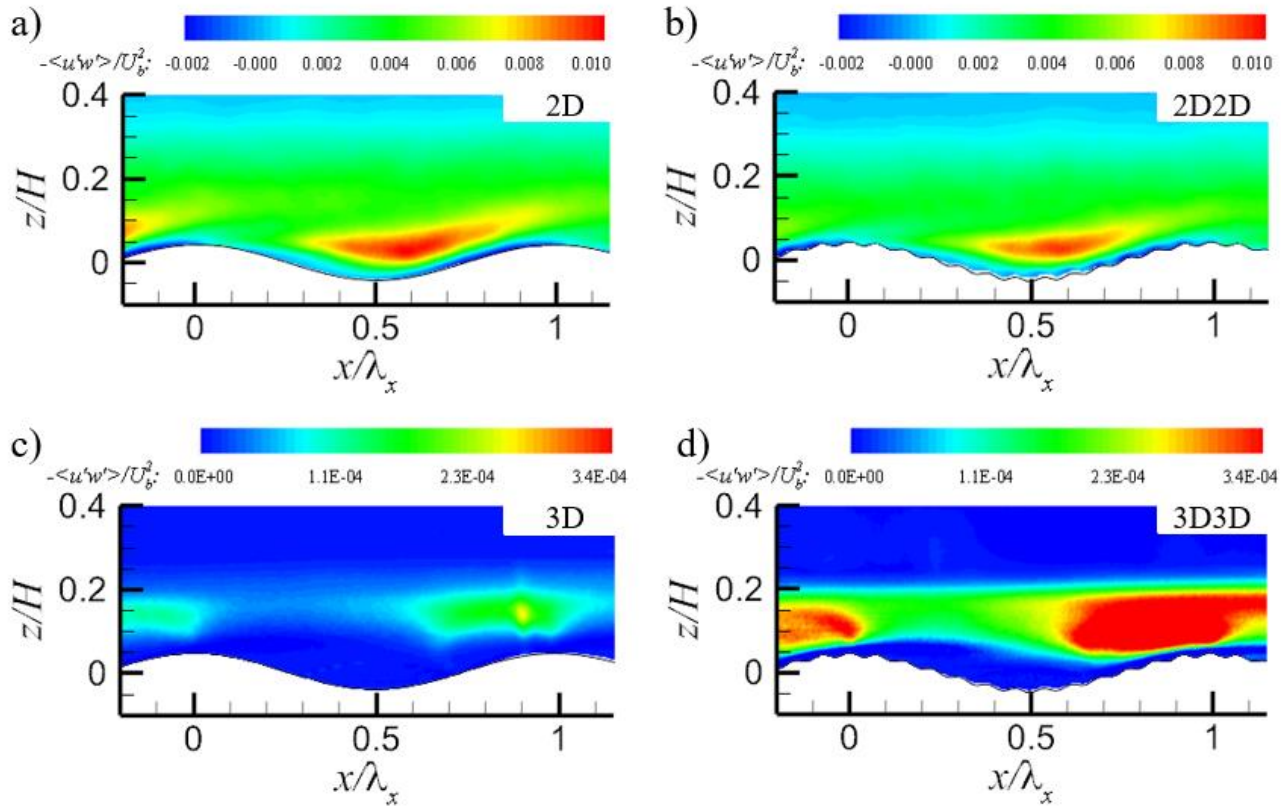

Figure 12: Turbulent kinetic energy $\boldsymbol{TKE} = \langle \boldsymbol{u'^2} + \boldsymbol{w'^2} \rangle / \boldsymbol{2U_b^2}$ fields of the a) 2D, b) 2D2D, c) 3D and d) 3D3D topographies, at Reynolds number of 4000.

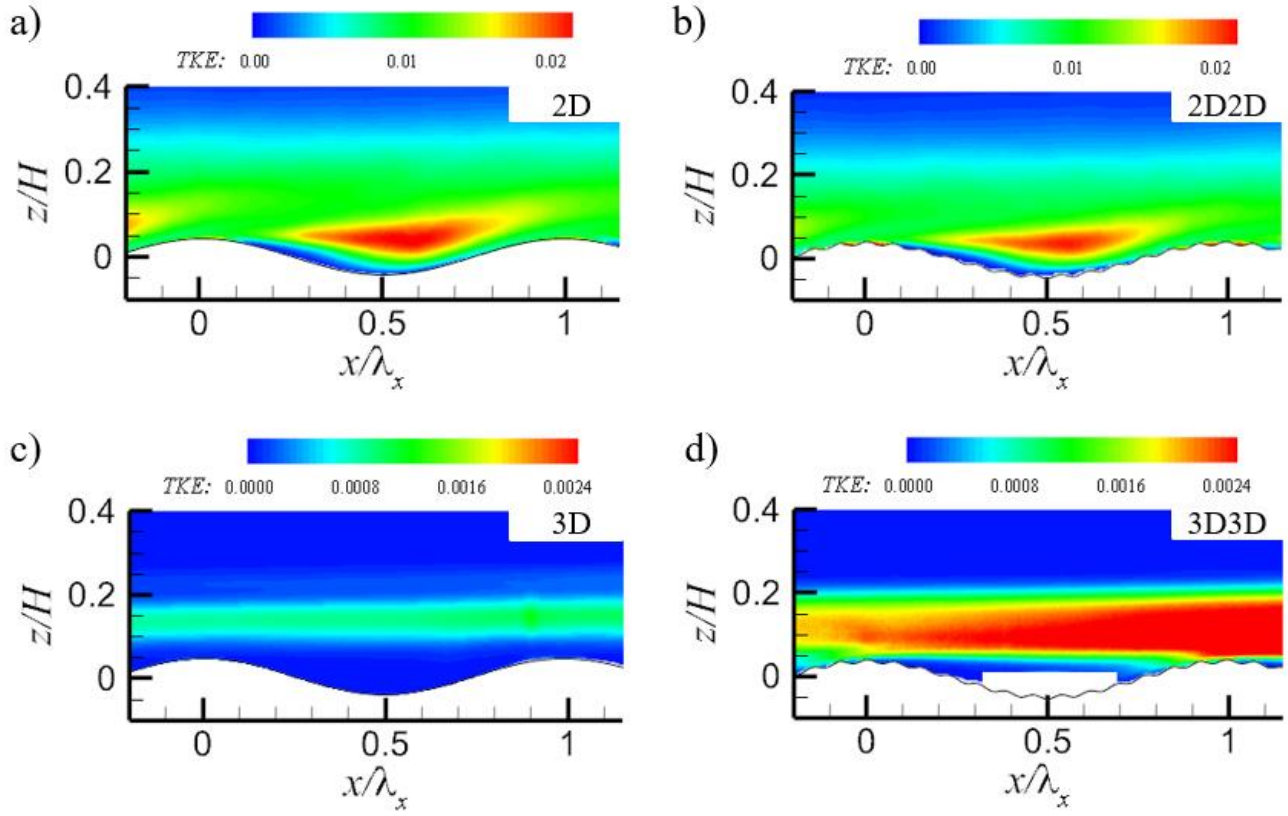

Figure 13: Turbulent kinetic energy production $\boldsymbol{E_{tk}}$: a) 2D, b) 2D2D, c) 3D and d) 3D3D topographies, at Reynolds number of 4000.

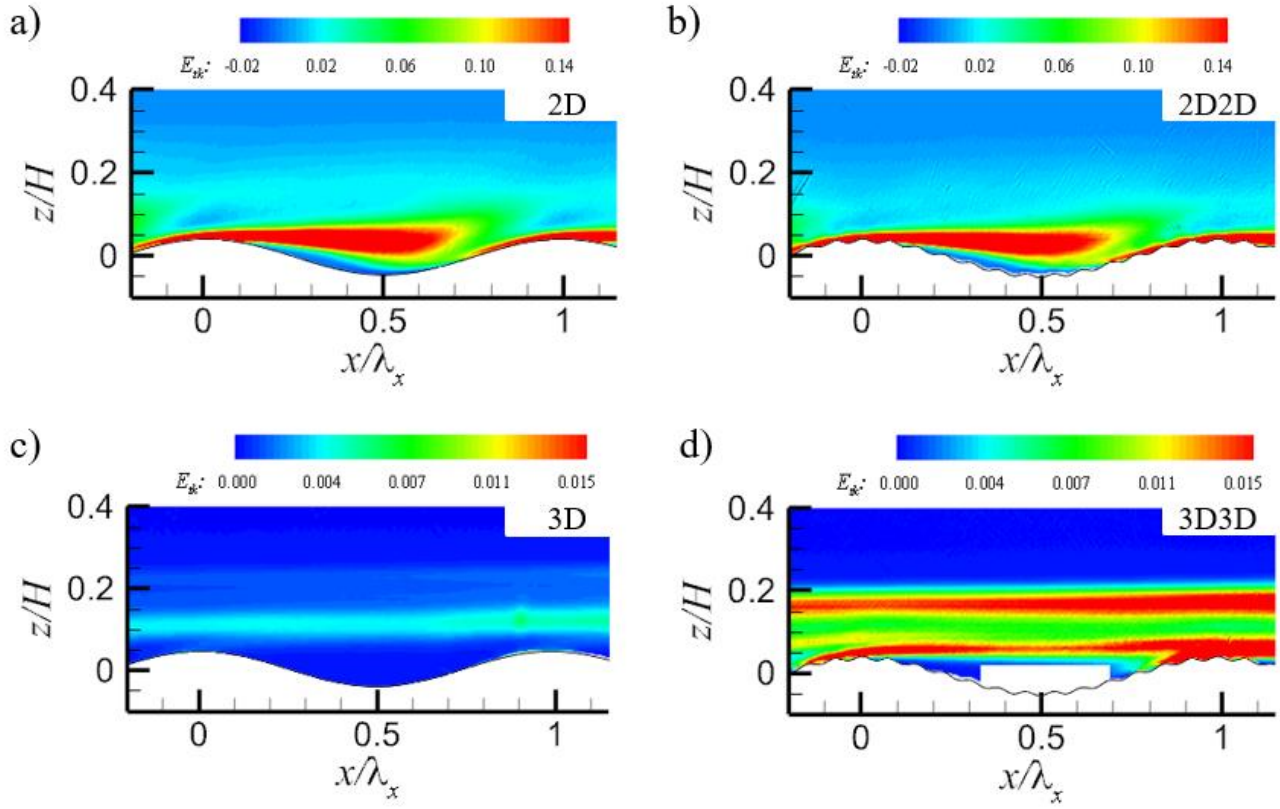

Figure 14: Non-dimensional time-averaged streamwise velocity profiles. 2D case in red and 2D2D case in black, at Reynolds number of 4000.

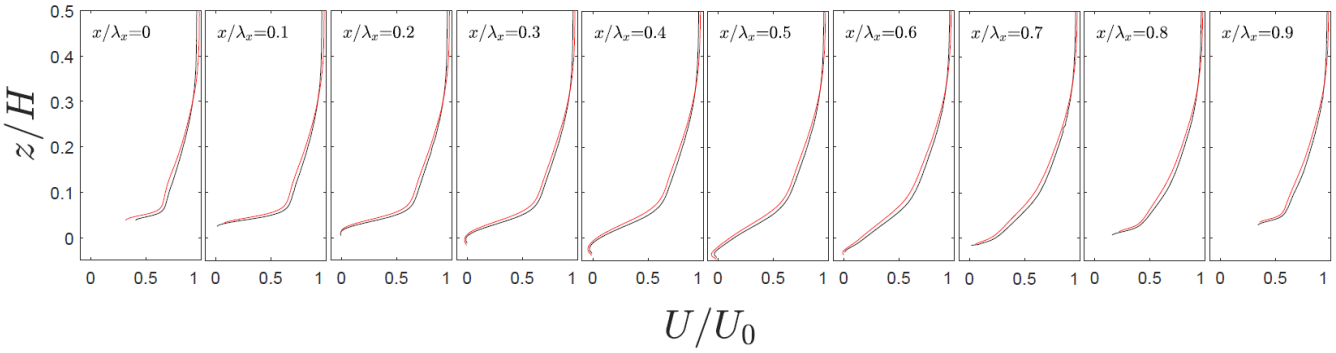

Figure 15: Non-dimensional time-averaged streamwise velocity profiles. 3D case in red and 3D3D case in black, at Reynolds number of 4000.

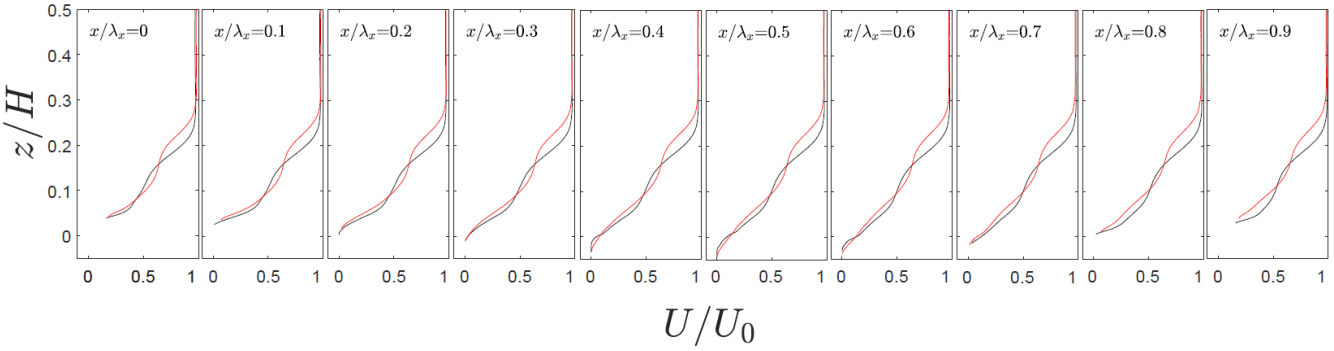

Figure 16: Non-dimensional time-averaged Reynolds shear stresses profiles. 2D case in red and 2D2D case in black, at Reynolds number of 4000.

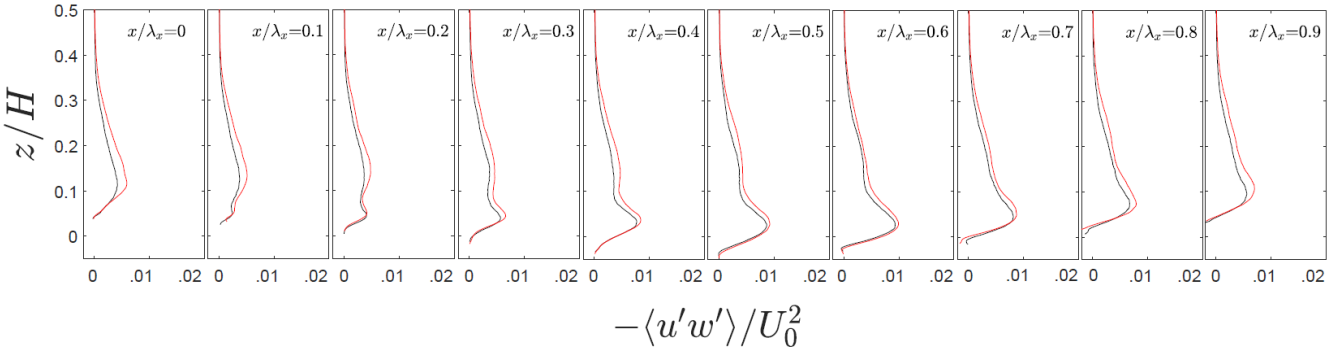

Figure 17: Non-dimensional time-averaged Reynolds shear stresses profiles. 3D case in red and 3D3D case in black, at Reynolds number of 4000.

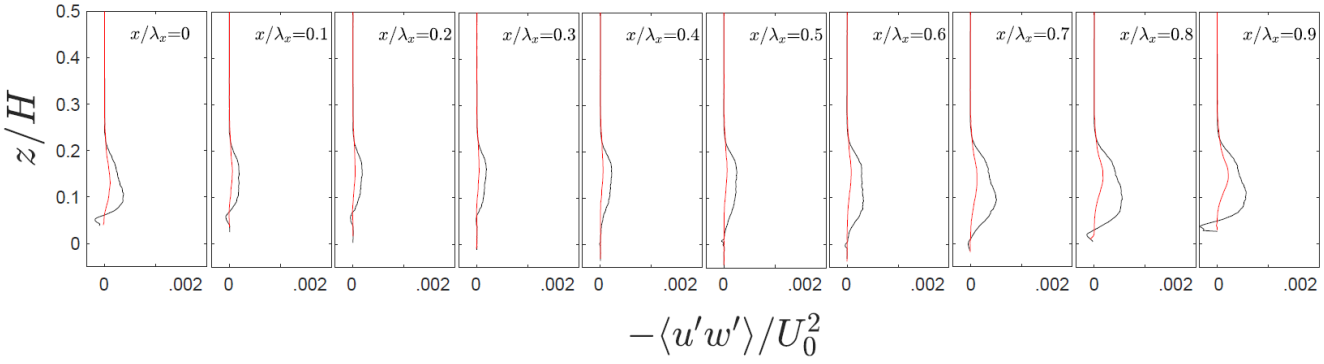

Figure 18: Non-dimensional time-averaged turbulence intensity profiles. 2D case in red and 2D2D case in black, at Reynolds number of 4000.

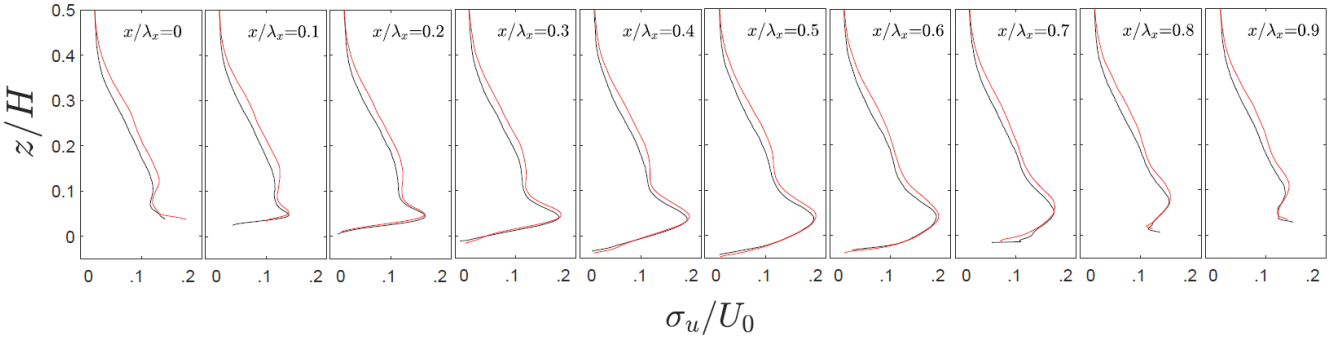

Figure 19: Non-dimensional time-averaged turbulence intensity profiles. 3D case in red and 3D3D case in black, at Reynolds number of 4000.

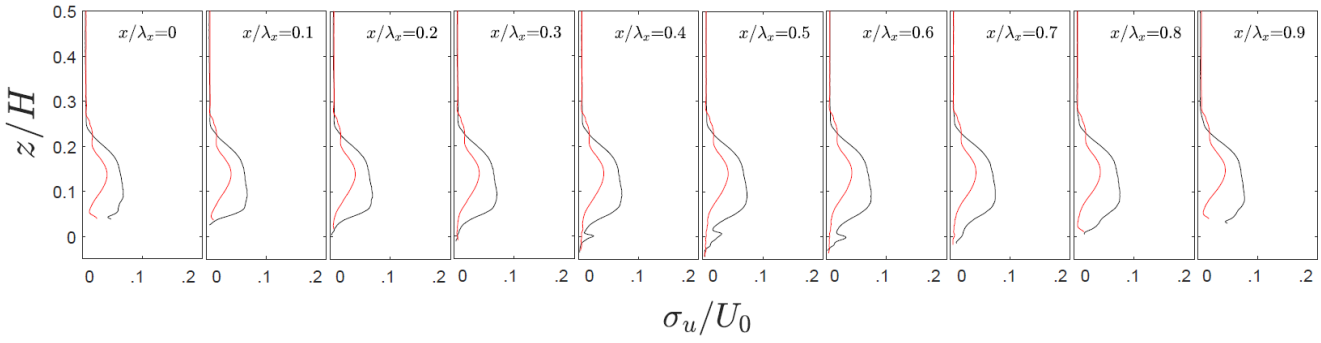

APPENDIX B: CASES AT REYNOLDS NUMBER OF 40000

Figure 20: Non-dimensional time-averaged spanwise velocity fields $\boldsymbol{W/U_b}$ of the a) 2D, b) 2D2D, c) 3D and d) 3D3D topographies, at Reynolds number of 40000.

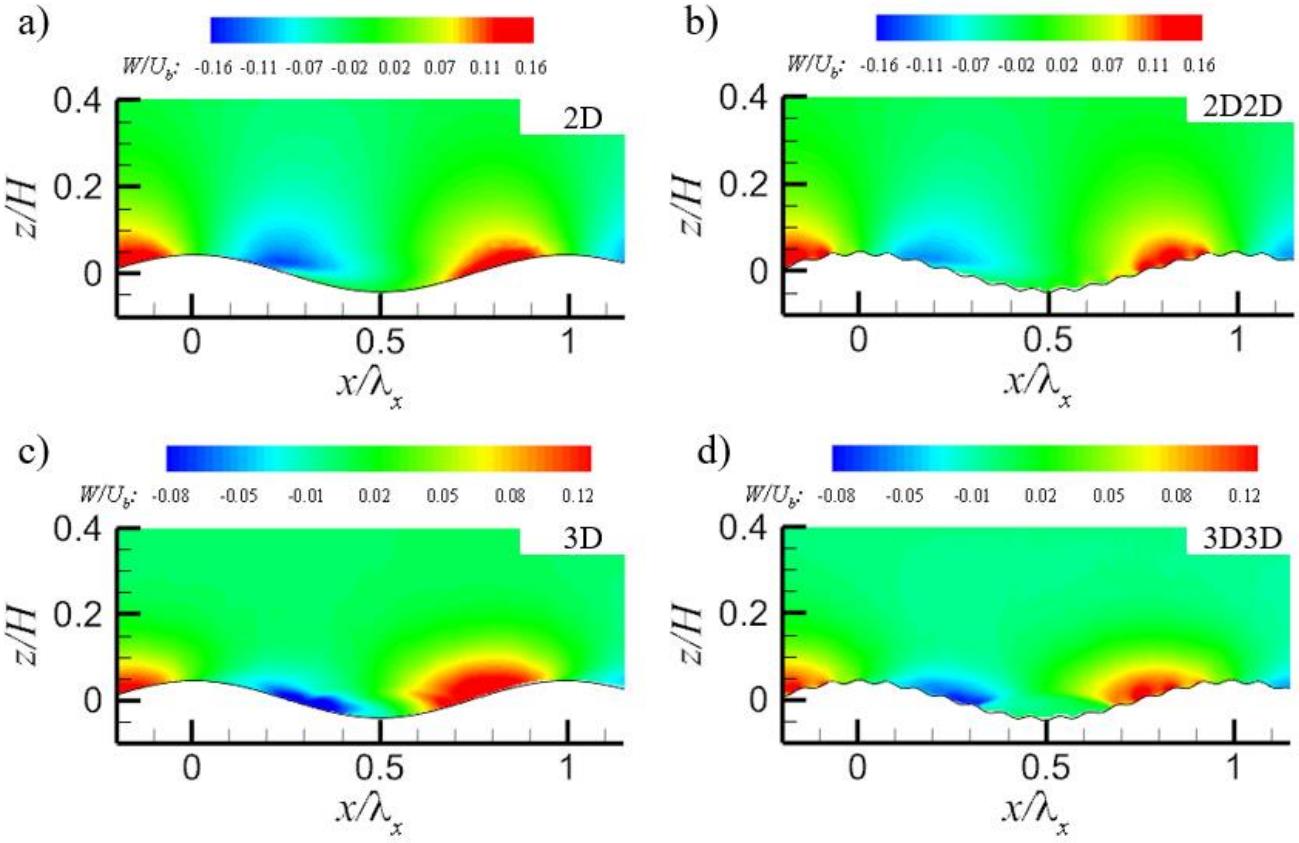

Figure 21: Reynolds shear stress $-\langle u'w'\rangle/U_b^2$ of the a) 2D, b) 2D2D, c) 3D and d) 3D3D topographies, at Reynolds number of 40000.

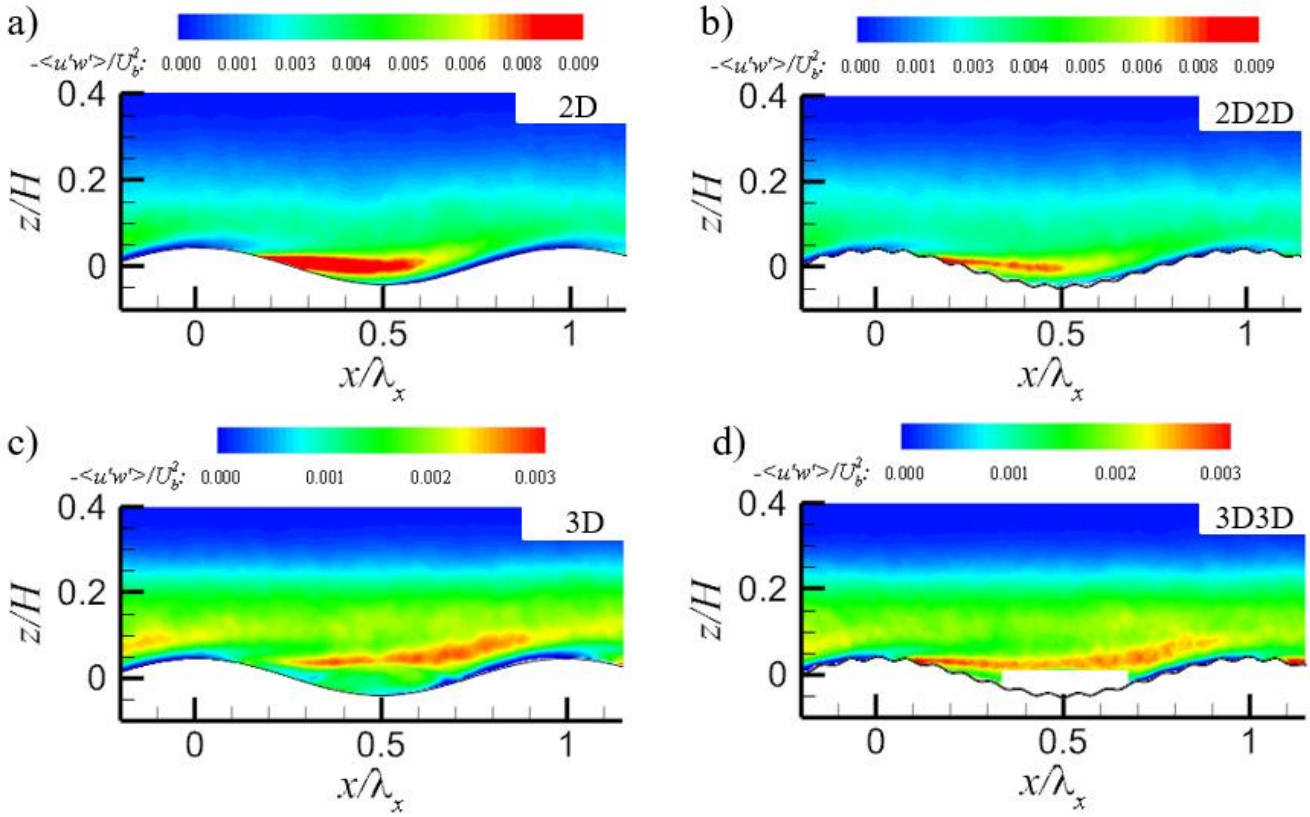

Figure 22: Turbulent kinetic energy $\boldsymbol{TKE = \langle u'^2 + w'^2 \rangle / 2U_b^2}$ fields of the a) 2D, b) 2D2D, c) 3D and d) 3D3D topographies, at Reynolds number of 40000.

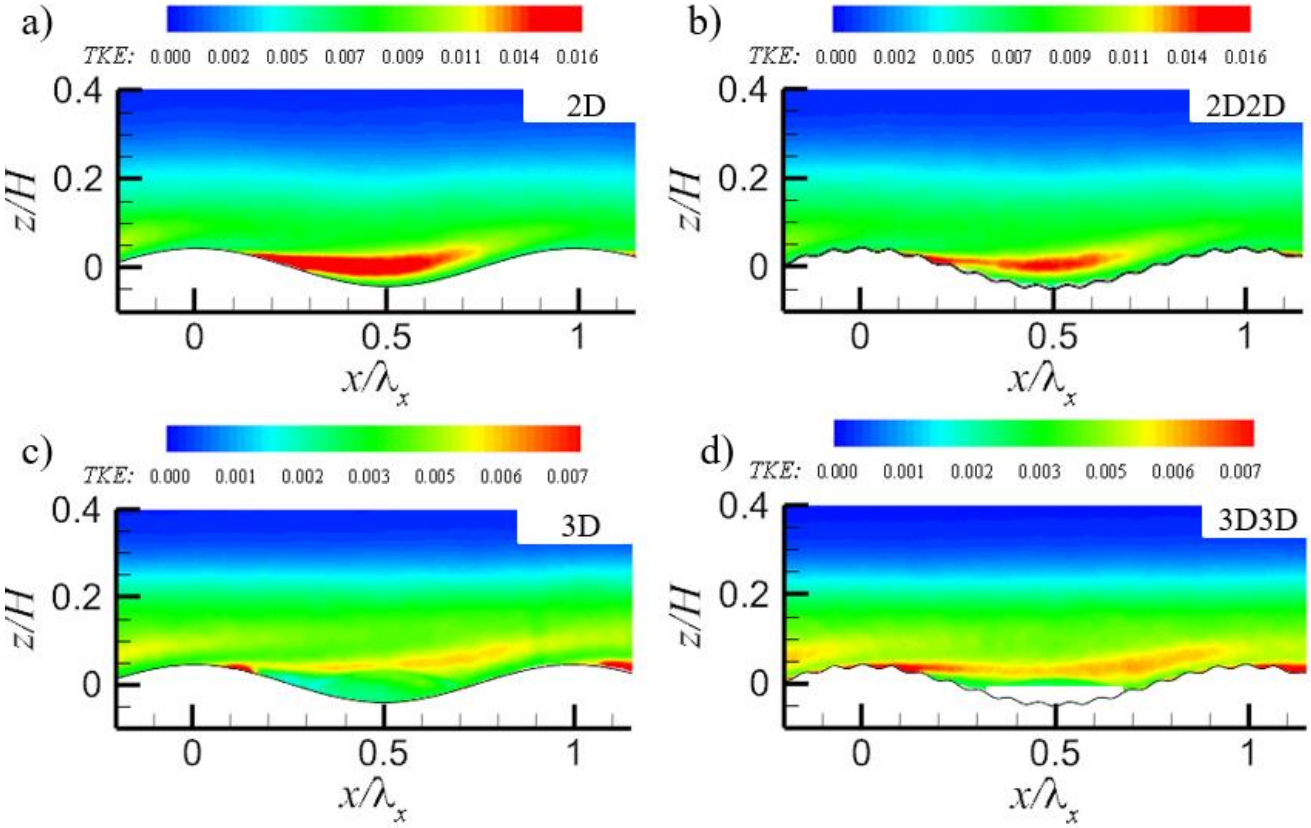

Figure 23: Component of the first mode, $\boldsymbol{\phi_{u'}}$, obtained from: a) 2D, b) 2D2D, c) 3D and d) 3D3D topographies, at Reynolds number of 40000.

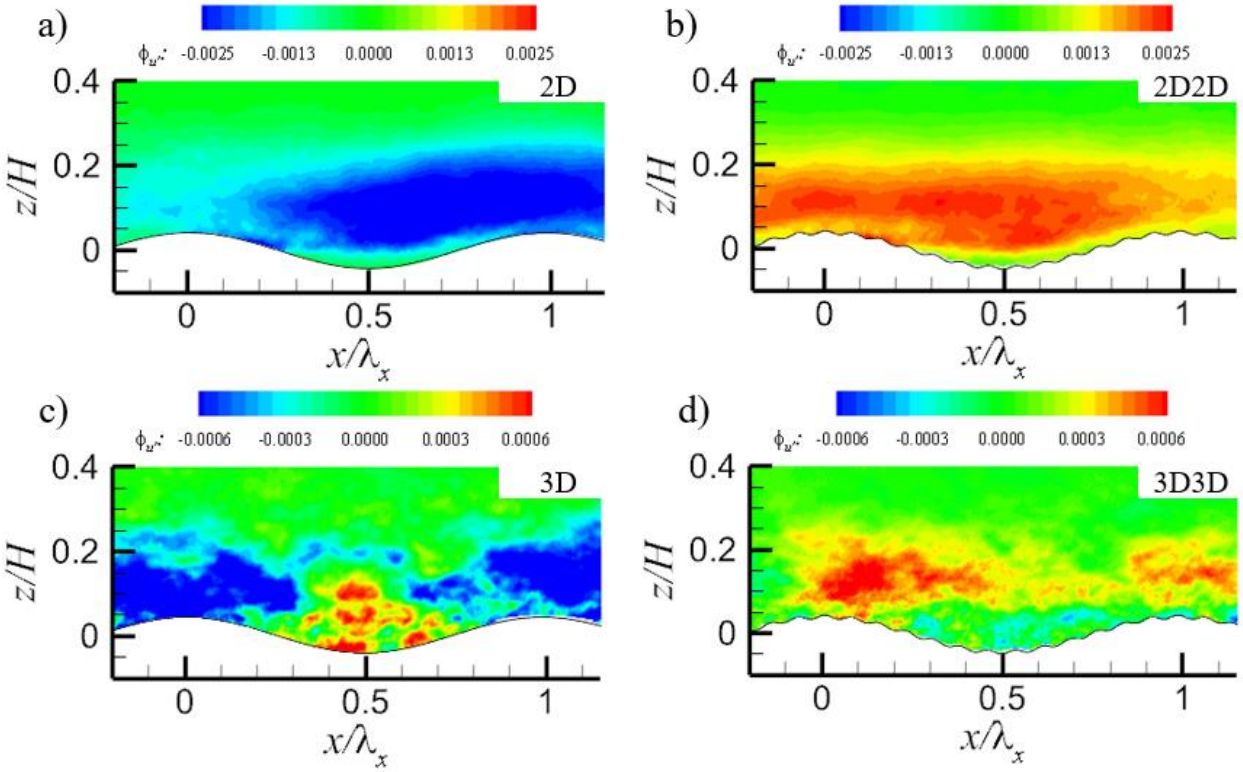

Figure 24: $\boldsymbol{\phi_{u'}}$ component of the fifth mode, obtained from: a) 3D and b) 3D3D topographies; and $\boldsymbol{\phi_{u'}}$ component of the tenth mode, obtained from: c) 3D and d) 3D3D topographies, at Reynolds number of 40000.

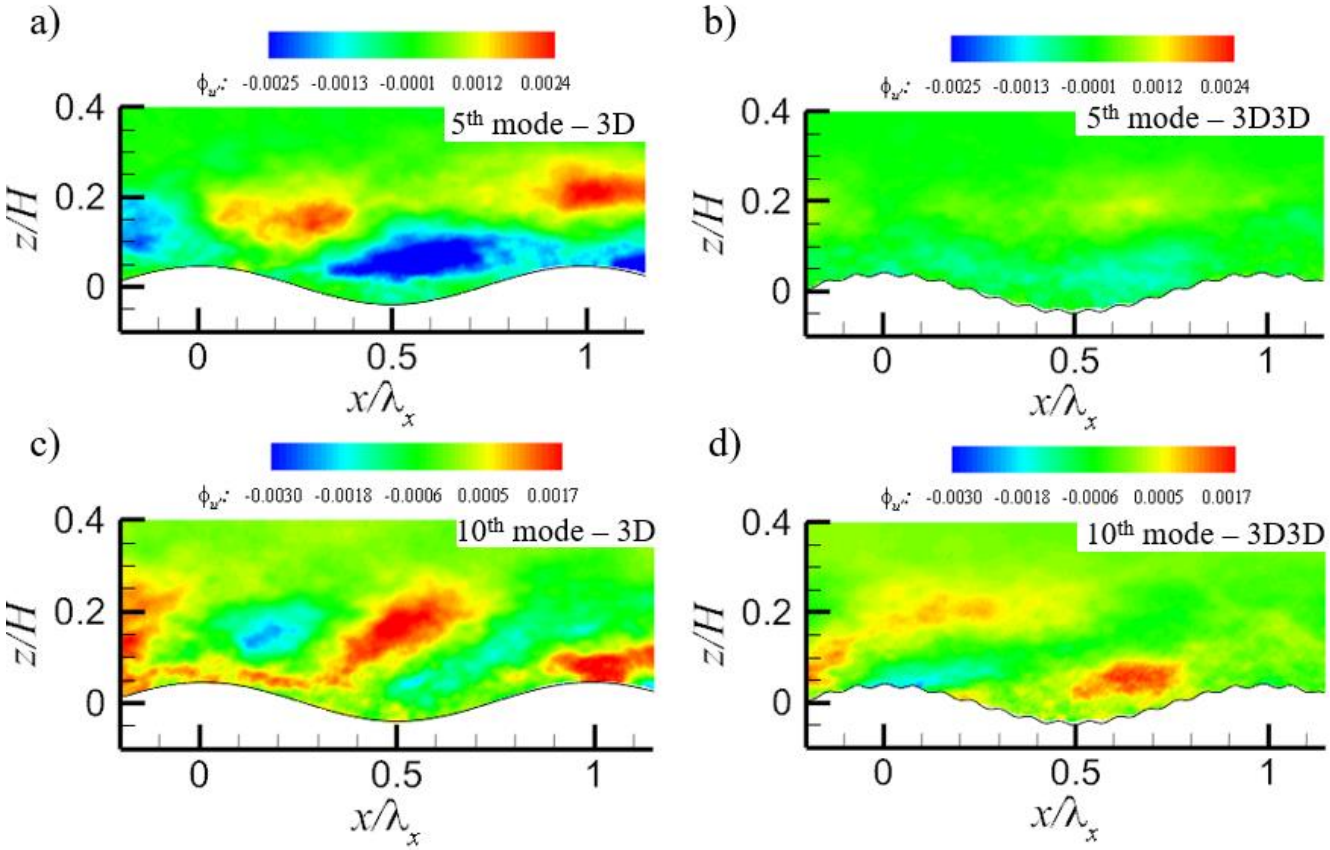

Figure 25: Quadrant decomposition of the kinematic shear stress $\boldsymbol{u'w'}$. Ejection events (Q2) for the a) 3D and b) 3D3D cases: sweeps (Q4) events for the c) 3D and d) 3D3D cases.

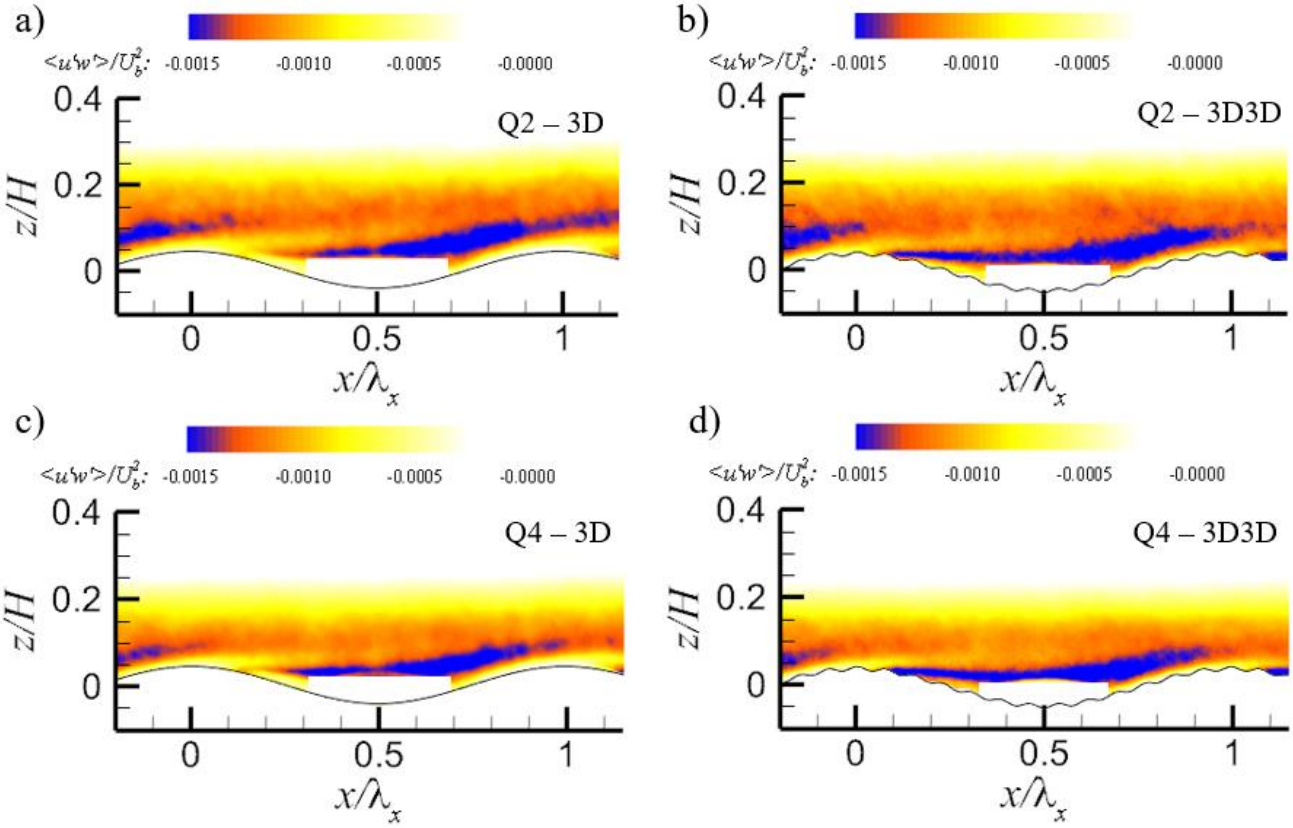

Figure 26: Profiles of the Reynolds stress $-\langle u'w' \rangle$ distribution, normalized by the shear velocity u_τ for: a) 2D, b) 2D2D, c) 3D and d) 3D3D topographies, at Reynolds number of 40000.